Integration of Spatial Distortion Effects in a 4D Computational Phantom for Simulation Studies in Extra-Cranial MRI-guided Radiation Therapy: Initial Results

C Kroll[a1], O Dietrich[b], J Bortfeldt[a,c], F Kamp[d], S Neppl[d], C Belka[d,e], K Parodi[a], G Baroni[f,g], C Paganelli[f] and M Riboldi[a2]

a. Department of Medical Physics, Ludwig-Maximilians University, Garching, 85748, Germany

b. Department of Radiology, University Hospital, LMU Munich, Munich, 81377, Germany

c. European Organization for Nuclear Research (CERN), 1211 Geneva 23, Switzerland

d. Department of Radiation Oncology, University Hospital, LMU Munich, Munich, 81377, Germany

e. German Cancer Consortium (DKTK), Munich, 81377, Germany

f. Dipartimento di Elettronica, Informazione e Bioingegneria, Politecnico di Milano, Milano, 20133, Italy

g. Bioengineering Unit, Centro Nazionale di Adroterapia Oncologica, Pavia, 27100, Italy

Short running title: Spatial distortions in a 4D MRI phantom

[1] Now working at Max Planck Institute for Meteorology, Hamburg, Germany
[2] Correspoding author. Address: Am Coulombwall 1, 85748 Garching b. München, Germany. E-mail: marco.riboldi@physik.uni-muenchen.de

This article has been accepted for publication and undergone full peer review but has not been through the copyediting, typesetting, pagination and proofreading process, which may lead to differences between this version and the Version of Record. Please cite this article as doi: 10.1002/mp.14611

Abstract (500 words)

Purpose. Spatial distortions in magnetic resonance imaging (MRI) are mainly caused by inhomogeneities of the static magnetic field, nonlinearities in the applied gradients, and tissue-specific magnetic susceptibility variations. These factors may significantly alter the geometrical accuracy of the reconstructed MR image, thus questioning the reliability of MRI for guidance in image-guided radiation therapy. In this work, we quantified MRI spatial distortions and created a quantitative model where different sources of distortions can be separated. The generated model was then integrated into a 4D computational phantom for simulation studies in MRI-guided radiation therapy at extra-cranial sites.

Methods. A geometrical spatial distortion phantom was designed in four modules embedding laser-cut PMMA grids, providing 3520 landmarks in a field of view of (345 × 260 × 480) mm^3. The construction accuracy of the phantom was verified experimentally. Two fast MRI sequences for extra-cranial imaging at 1.5 Twere investigated, considering axial slices acquired with online distortion correction, in order to mimic practical use in MRI-guided radiotherapy. Distortions were separated into their sources by acquisition of images with gradient polarity reversal and dedicated susceptibility calculations. Such a separation yielded a quantitative spatial distortion model to be used for MR imaging simulations. Finally, the obtained spatial distortion model was embedded into an anthropomorphic 4D computational phantom, providing registered virtual CT/MR images where spatial distortions in MRI acquisition can be simulated.

Results. The manufacturing accuracy of the geometrical distortion phantom was quantified to be within 0.2 mm in the grid planes and 0.5 mm in depth, including thickness variations and bending effects of individual grids. Residual spatial distortions after MRI distortion correction were strongly influenced by the applied correction mode, with larger effects in the trans-axial direction. In the axial plane, gradient nonlinearities caused the main distortions, with values up to 3 mm in a 1.5 T magnet, whereas static field and susceptibility effects were below 1 mm. The integration in the 4D anthropomorphic computational phantom highlighted that deformations can be severe in the region of the thoracic diaphragm, especially when using axial imaging with 2D distortion correction. Adaptation of the phantom based on patient-specific measurements was also verified, aiming at increased realism in the simulation.

Conclusions. The implemented framework provides an integrated approach for MRI spatial distortion modeling, where different sources of distortion can be quantified in time-dependent geometries. The computational phantom represents a valuable platform to study motion management strategies in extra-cranial MRI guided radiotherapy, where the effects of spatial distortions can be modeled on synthetic images in a virtual environment.

Keywords

spatial distortion artefacts, image guidance, MRI-guided radiotherapy, magnetic field inhomogeneity, gradient nonlinearities, susceptibility

1. Introduction

The use of Magnetic Resonance Imaging (MRI) in external beam radiotherapy is rapidly increasing, with a clear potential to provide guidance for treatment planning, treatment delivery and response assessment (1-3). Recent developments have resulted in commercial availability of linear accelerators with an integrated MRI unit, thus allowing the implementation of fully magnetic resonance-guided radiotherapy (MRgRT) protocols (4). In the treatment of moving targets, MRgRT provides superior soft-tissue contrast at no cost in terms of ionizing radiation, along with the benefit of fast imaging sequences (5, 6). This entails significant advantages, allowing extended image acquisitions to take into account respiratory motion and its cycle-to-cycle variations (7, 8). Furthermore, the ability to image at high repetition rates during treatment yields the possibility to implement MR-guided motion management strategies (5). Current approaches for motion management in MRgRT rely on respiratory gating, based on a 2D cine-MRI image acquired across the tumor area (9). On the other hand, the ability to image anatomical changes, including variations in motion patterns for moving targets, opens the possibility to adapt treatment delivery (10, 11).

In light of such possibilities, the validation of complex motion management strategies in MRgRT does require the use of dedicated phantoms. Different designs have been proposed, including both physical and

computational phantoms. Physical 4D phantoms for use in MR imaging have been developed relying on either ex-vivo lung models (12-14), or on custom developments to create inflatable synthetic lung structures (15, 16). Conversely, there is an increasing interest in computational phantom models to provide simulations for different applications in life science, including imaging (17-19). As far as motion management in MRgRT is concerned, computational phantoms provide the ability to simulate different MR sequences, with a time-resolved ground truth anatomical representation that can overcome current limitations in MR image acquisition (20, 21). As motion management in MRgRT entails image reconstruction, processing and segmentation, these phantoms can be exploited to compare with respect to a time-resolved volumetric ground truth (22). This is of particular interest for motion management, as the volumetric ground truth can be exploited for in-silico testing of different k-space sampling strategies for image acquisition speed-up and reduction of artefacts (5, 6, 23). They are therefore expected to be an extremely useful tool, complementing experimental verification with physical phantoms.

Current developments toward the implementation of computational phantoms featuring the ability to simulate MR imaging rely on the ongoing efforts to develop realistic phantoms for dosimetry (18, 19). Specifically, most of these developments are based on adaptations of the 4D XCAT phantom, which was originally designed to simulate time-resolved Computed Tomography (CT) and nuclear imaging (24). One possibility to modify the 4D XCAT for the simulation of MR imaging is to exploit the activity mode, i.e. with organ-defined activity values, to express idealized MR signal intensities (25). A different approach by Wissmann et al. entails the specific inclusion of MR sequence signal modeling, as well as tissue-specific relaxation times and proton densities (26). Both approaches have been tested for applications in cardiac imaging (25, 26). As an alternative technique, the MR signal intensity can be derived by solving the Bloch equations directly, which allows one to model time dependent effects such as the use of contrast agents (27).

Based on the approach by Wissmann et al, a 4D CT/MRI Breathing Anthropomorphic Thorax phantom (CoMBAT) has been developed for applications in MRgRT (22). The phantom includes tissue parameters derived from experimental acquisitions, expressing the proton density and relaxation times (T1 and T2) for the main tissues in abdominal imaging. Using these parameters, the acquisition of different MR sequences can be simulated, taking into account the MR signal model, the coil sensitivity and the implemented raw data acquisition (k-space sampling). The CoMBAT phantom is therefore able to generate CT and MR images that

are perfectly co-registered, providing simulated data at null registration error. The phantom however fails to include MRI-induced spatial distortions, which are particularly important when the geometrical characterization of the patient anatomy is essential, as in the case of MRgRT.

Spatial distortion artefacts are caused by magnet-related static field inhomogeneities (B_0 inhomogeneities), by nonlinearities in the magnetic field gradients, which are specific for each MR acquisition sequence, and by tissue-dependent magnetic field variations due to the intrinsic magnetic susceptibility. Spatial distortion artefacts, especially those which are temporally varying as a consequence of motion, can lead to the erroneous implementation of motion management strategies in MRgRT (5, 6). The overall effect of spatial distortions in MRI has been studied both for known geometries (28, 29) and unknown structures (30). Stanescu and Jaffray specifically investigated the 4D composite MR image distortion field associated with tumor motion in MRgRT (31). They concluded that system-related distortions, due to static field inhomogeneities and gradient nonlinearities, are the dominant component, while susceptibility-induced effects are minimal for high read-out gradients, as typically applied in dynamic MR imaging.

In this work, we describe the development of a 4D computational MRI phantom that includes the simulation of spatial distortions effects, to be used for the evaluation of MR-based motion management in MRgRT. Experimental measurements in a custom-made distortion phantom are reported, providing the quantification of system-related distortions, namely B_0 inhomogeneities and gradient nonlinearities. These measurements are processed to derive a spatial distortion model, as complemented by numerical simulation of susceptibility effects (32). The developed methodology is tested on two specific 2D pulse sequences: the spoiled gradient-echo (sGRE) and the balanced steady-state free-precession (bSSFP). We show that the derived model can provide a realistic simulation that includes spatial distortion effects, and that those effects can be separated into individual contributions.

2. Materials and Methods

We quantified spatial distortions relying on MR measurements of a custom-made distortion phantom, as detailed in the flowchart depicted in Figure 1. Spatial distortions were quantified by image registration of acquired MR images with a virtual digital model of the phantom. MR images were acquired with different polarities of the gradients, in order to separate gradient-based contributions from spatial distortions due to static field inhomogeneities and susceptibility. Susceptibility-induced effects were simulated on the CoMBAT phantom reference anatomy, as detailed in Kroll et al. (32). Distortions due to susceptibility were calculated by solving Maxwell's equation in the CoMBAT reference anatomy, relying on tabulated values for the volume susceptibility of different tissues (32). The combined and separated spatial distortion components were finally integrated into the CoMBAT phantom (22), thus providing a complete simulation framework to analyze MRI distortion effects in MRgRT.

FIGURE 1

2.1. Phantom construction and quality assessment

For spatial distortion assessment, a four-modular phantom made from polymethylmethacrylat (PMMA) with outer dimensions of (369 × 300 × 500) mm^3 was designed, as shown in Figure 2. Each of the four modules hosts five distortion grids with distinct geometrical structures (possible landmarks) at each grid intersection, making 3520 landmarks in total. The modules can be filled with water or a contrast agent solution to provide the required MR signal. The phantom was placed on a 112 mm high PMMA table in order to guarantee a flat and stable support in the MR scanner, which could be hardly achieved with conventional supports. As additional benefits, the PMMA table allowed us to mimic the vertical patient offset during radiation treatment due to immobilization devices, and define very precise boundary conditions when considering susceptibility-induced effects.

FIGURE 2

Along with the physical phantom, a virtual matrix model of the distortion phantom was created according to the construction plan, relying on Matlab (The MathWorks, Inc., Natick, MA). The virtual model was used for image registration purposes, allowing a comparison of the acquired images with the ideal phantom geometry.

After construction, the geometric accuracy of the phantom was determined using a combination of three methods:

- A laser tracking system (Hybrid Polaris Spectra, Northern Digital Inc., accuracy within ±0.2 mm) and caliper measurements (±0.05 mm precision) were used to quantify the grid spacing and to check the correct size of each component.
- The PMMA plate flatness was measured relying on a laser triangulation system. An optical non-contact displacement transducer with blue light option from micro-epsilon (model με optoNCDT ILD 2300-2BL) was used for measurements, providing an accuracy of ≈6 μm over the entire surface.
- CT images were acquired with a CT scanner (Aquilon LB, Canon Medical Systems, Japan), with the standard protocol for abdominal imaging at a resolution of (1.074 × 1.074 × 1) mm^3. They were used to evaluate the combined error of the deformations caused by phantom imperfections and image registration errors. For this latter purpose, a registration of the CT images with a virtual model of the phantom was performed as described in section 2.3. The landmark position at the grid intersections were determined by convolving the 3D CT image with a 3D matrix representing one grid intersection. From the convolution result, the regions of highest signal (maximum overlap) were used to calculate the position of the landmarks. Then the distance between the landmarks on the grid intersections of the virtual phantom, warped with the registration results (see section 2.3), and the landmarks as determined in the CT images was quantified. As described later, the root mean square deviation (RMSD) of the determined distances was taken as an error in the MR image analysis.

The phantom was filled with distilled water for measurements inside the MR scanner. In order to remove air bubbles, which formed when filling the phantom due to turbulence and the electrostatic characteristics of the PMMA, an air removal procedure was developed (Figure 3). Specifically, the phantom is filled with water leaving a few millimeters unfilled. Then the phantom is positioned in a vacuum chamber as shown in Figure 3, leaving the filling openings unplugged and the vacuum chamber closed subsequently. The pressure is decreased to approximately (39 − 45) mbar, while avoiding to approach the vapor pressure curve too closely. The phantom is left within the vacuum chamber at decreased pressure for about 15 min and then slowly re-accommodated to atmospheric pressure. Now the phantom can be filled completely with water, using water which has undergone the same procedure as the phantom. The phantom is left standing open for a couple of hours in order to allow regaining of equilibrium conditions, including the resaturation of the water with oxygen. Then the phantom openings are closed.

FIGURE 3

2.2. MR data acquisition

MR images of the static distortion phantom on the 112 mm high PMMA table were acquired using a 1.5 T scanner (Magnetom Aera, Siemens Healthineers, Erlangen, Germany) with a 70 cm bore and a high-performance gradient system (45 mT/m, 200 T/m/s). Two 2D pulse sequences were chosen, which are commonly used for capturing the breathing motion dynamics (5): the spoiled gradient-echo (sGRE) and the balanced steady-state free-precession (bSSFP) sequence. The sequence parameters are summarized in Table 1. For each sequence, two image sets were acquired by changing the gradient polarity in the frequency-encoding *x*- and phase-encoding *y*-direction between both runs. The polarity of the slice-selection gradient and all other parameters were left unchanged. The distortion correction for gradient non-linearities provided by the vendor was applied to both sequences, in order to acquire images with distortion levels that could be realistically expected during clinical practice. Our measurements were therefore focused on residual distortions, following distortion correction. The distortion correction methods available on the scanner console were applied: 2D for bSSFP and 3D for sGRE.

TABLE 1

2.3. Image registration

CT and MR images were registered with a virtual matrix model of the used distortion phantom in a two-step process, involving rigid image alignment followed by a deformable registration procedure. In a first step, purely translational and rotational misalignment between the image and the virtual phantom was removed in a rigid registration procedure (6 DOF) using 3D Slicer (version 4.8.0) (33) with the default metric settings. In a subsequent step, a deformation matrix was extracted relying on a deformable image registration (DIR) procedure. Depending on the image contrast, noise level, and artefacts, the metric was chosen. For the CT images, a B-spline interpolation with a mean square error metric (*mse*) by Plastimatch (34) was used. In the case of sGRE images, the B-spline interpolation of Plastimatch was applied with the mutual information metric (*mattes*), whereas REGGUI (35) was used for the bSSFP images with the Morphons algorithm and

default parameters. The deformation field was evaluated to gain information on: (i) the phantom construction inaccuracies and the error in the registration process in case of the CT images, (ii) the image deformations in case of the MR images.

2.4. Reversed gradient method

In order to separate the different spatial distortion contributions in the MR image, the reversed gradient method (36) was applied. As Bakker *et al* did not account for susceptibility effects, the corresponding term was added to the used algorithm (37, 38).

The deformation fields of two images with identical parameters, except for the gradient polarity, are used. The change of gradient polarity leads to a sign change of the deformations caused by static B_0 inhomogeneities and susceptibility effects in the frequency-encoding *x*-direction, while the gradient-induced distortions remain unchanged. Therefore for a 2D sequence with frequency encoding in the *x*-direction and phase encoding in the *y*-direction, the reallocation of an object at position *(x,y,z)* to position ($x'^{\pm}$,$y'^{\pm}$,$z'^{\pm}$) is given by:

$$x'^{\pm} = x + \frac{dB_{G_x}(x,y,z)}{G_x} \pm \frac{dB_0(x,y,z)}{G_x} \pm \frac{dB_\chi(x,y,z)}{G_x} \text{ (frequency-encoding direction, gradient reversal)} \quad (1)$$

$$y'^{\pm} = y + \frac{dB_{G_y}(x,y,z)}{G_y} \quad \text{(phase-encoding direction, gradient reversal)} \quad (2)$$

$$z'^{\pm} = z + \frac{dB_{G_z}(x,y,z)}{G_z} + \frac{dB_0(x,y,z)}{G_z} + \frac{dB_\chi(x,y,z)}{G_z} \text{ (slice-selection direction, no gradient reversal)} \quad (3)$$

where G_i is the (imaging) gradient in direction *i* with $i \in \{x,y,z\}$, $\mathrm{dB_0(x,y,z)}$ are the magnetic field changes caused by static B_0 inhomogeneities, $dB_{G_i}(x,y,z)$ the field changes caused by gradient nonlinearities, and $dB_\chi(x,y,z)$ the field changes caused by susceptibility effects. Addition and subtraction of the deformation fields allows separating the gradient-induced deformations from the B_0 and susceptibility-induced effects in the *x*-direction. The above formulas have been developed for uncorrected MR images, but were applied to

distortion-corrected images in this work: the validity of this assumption is discussed later in the text (section 4.4).

2.5. Analysis of spatial distortion

As the MR images were heavily distorted in the outer image regions, the analysis was restricted to a smaller volume containing the two central modules. In addition, the volume was selected individually for the two analyzed sequences, depending on the visibility of phantom landmarks: the extent of such a volume is represented in Figure 6. The total distortion in each direction, as well as the specific contributions calculated with the reversed gradient method (see section 2.4) were statistically compared in the area intersecting the volumes defined for the bSSFP and sGRE sequences (Figure 6). The spatial distortion was compared at the landmarks defined in the spatial distortion phantom, for a total of 1460 landmarks over 10 axial slices. The distortion in the two sequences was compared statistically relying on the Wilcoxon text for matched pairs, considering either the overall set of landmarks, or the single axial slice individually. A confidence of 99% was applied in the evaluation of the statistical analysis.

2.6. Implementation in the CoMBAT phantom

The image deformations due to B_0-inhomogeneities, gradient nonlinearities and susceptibility effects were implemented in CoMBAT by warping the MR images with the corresponding deformation fields. The original CoMBAT tool (22) simulates the MR image acquisition using a 4D anthropomorphic thorax phantom (24). For this purpose, the digital phantom, described by the matrix $O(\vec{x},t)$, is translated into k-space according to:

$$O(\vec{k},t) = \sum_{i=1}^{N,S} R\,[F\,S(N_{coil})C(T_E, T_R,\alpha)\,T(T_1,T_2,\rho)O(\vec{x},t) + n(\vec{k},t)] \qquad (4)$$

In the above equation, starting from the digital time-space domain phantom $O(\vec{x}, t)$, MR parameters for the tissue dependent relaxation times and proton densities are defined by $T(T_1, T_2, \rho)$. Different relaxation times

and proton densities are simulated according to the corresponding $T_1, T_2$and ρ characteristics, which are assumed to be known for each tissue (i.e. at each spatial location). The MRI signal sequences are then described by the operator $C(T_E, T_R, \alpha)$. The MR signal is recorded by the individual readout coils: to simulate these steps, the signal is multiplied by the spatially-varying sensitivities of these respective coils given by $S($ N_{coils}) and then the recorded signal is Fourier transformed using F. A Gaussian noise contribution $n(\vec{k}, t)$ is added to the recorded signal after the total signal is transformed into the k-space domain (39). In the final step, the sampling of the k-space is done by using the readout function R: the user can adjust the corresponding parameters to the sequence to be simulated (39). Then the actual images are reconstructed as the inverse Fourier transform of $O(\vec{k},t)$. An isotropic resolution of 1 mm^3 voxel size was utilized for the 4D volume reconstruction, and subsequently scaled to reproduce the image resolution used in the tested MR sequences (1.17 x 1.17 x 5 mm^3, see Table 1).

By integrating spatial distortions within the CoMBAT phantom, the user can choose to investigate the image deformation due to static B_0, gradient, and susceptibility effects, the sole contributions due to gradients effects in *x*-direction or *y*-direction, the sole contributions due to static B_0 and susceptibility effects in *x*-direction or the susceptibility effects in the direction of the static magnetic field. To calculate the susceptibility-caused deformations, these were determined according to the procedure described in (32).

In order to demonstrate the use of the phantom to reproduce clinical data, patient-specific phantoms were generated, as described in (21). Two lung cancer cases were selected: P01 featuring 6.3 mm peak to peak tumor motion, 9.6 mm diaphragm motion and 2.4 mm chest-wall expansion. The second case (P02) exhibited 8.1 mm tumor motion, 11.8 mm diaphragm motion and larger chest-wall expansion (9.6 mm). The tumor shape was segmented on the treatment planning 4D CT scan, relying on the exhale phase, whereas motion was estimated from the acquisition of cine-MR images at 300 ms frame rate (21). Clinical data were exploited to generate patient-specific phantom images, i.e. reproducing the exact tumor shape and the measured motion amplitudes. Finally, the patient-specific phantoms were warped with the vector field reproducing all spatial distortion effects, and then reconstructed at variable signal to noise ratio (SNR).

3. Results

3.1. Phantom quality assessment

The quality assessment of the phantom grids revealed a manufacturing accuracy ≤ 0.2 mm in plane and values below 0.5 mm in depth, which includes thickness variations and bending effects for the single grid units. These values were in accordance with the commonly reported accuracies of commercial phantoms, listed to be below 1 mm.

The RMSD of the phantom landmarks in the CT image and the virtual model after registration was found to be 1.00 mm for a registration based on the two central phantom modules at an image resolution of $(1.074 \times 1.074 \times 1)$ mm^3. The RMSD encompasses both the geometrical inaccuracy of the phantom and the registration inaccuracies. As such error estimate corresponded to the intrinsic image resolution (i.e. the smallest detectable distance), we assumed 1 voxel error bar in the following MR image analysis. The calculated RMSD value was therefore scaled according to the image resolution of the generated MR images (1.2 x 1.2 x 5 mm^3) and used as an error measure for the following registrations. This led to a direction-dependent error with smaller values for the in plane *x*- and *y*-directions and larger errors for the slice selection direction (*z*-direction).

3.2. Deformation fields of MR images

The image deformations and signal losses in the volume of the first and last static phantom module were so severe that the corresponding image slices were classified to be unsuitable for MRI-guided radiation therapy. The MR images discussed in the following sections are restricted to the volume of the two central phantom modules, covering a field of view of (345 × 260 × 230) mm^3 (Figure 4). This matches the volume typically acquired for MR-guidance. An increased artefact level and signal loss in the upper right and left corner of the images were found here as well, corresponding to the areas at the extreme outer regions of the MRI scanner bore. We therefore considered a smaller region of interest and cut out the areas of higher artefact level and signal loss (Figure 4). The bSSFP sequence exhibited larger portions of the image showing significant degradation, resulting in a smaller region where residual deformations could be quantified. This resulted in a total number of visible landmarks of the spatial distortion phantom equal to 1460 (146 per grid) for sGRE and 1620 (162 per grid) for bSSFP. In the corresponding areas of interest the maximum total 3D deformation for the sGRE and bSSFP sequence were 6.5 mm and 10.1 mm, the mean and standard deviation were determined

to be (2.6 ± 0.6) mm and (4.0 ± 2.0) mm. The distribution of the Jacobian determinants of the deformation vector fields resulted in all positive defined values, with maxima at 1.3 for sGRE and 1.8 for bSSFP.

FIGURE 4

The analysis of the deformation fields from the deformable image registration are shown in Figure 5. Thanks to the gradient reversal in the *x*-direction, contributions could be partially separated using the reversed gradient approach, as shown in the upper and central panels for the sGRE and the bSSFP sequence, displaying the B_0 and susceptibility effects separated from the gradient effects and vice versa. The last panel shows the deformations in the *z*-direction. The errors for the upper and central graphs were determined using the errors calculated in the CT image analysis and scaled to the MR image voxel size. The errors in the lower panel are the differences in the deformation level between the conventional and reversed gradient acquisition. The statistical analysis in the overlap region (Wilcoxon text for matched pairs) showed a statistical significant difference for the deformation contributions in the *x* and *y*-direction but not in the *z*-direction (p-value = 0.76). When the analysis was repeated for each single slice individually, results show that deformations in the *z*-direction are not significantly different in the center of the FOV (grid #10, central region in Figure 5, bottom panels), but indeed statistically different in the other slices.

FIGURE 5

3.3. Implementation in the CoMBAT phantom

The results of the distortion implementation in the CoMBAT phantom are visualized in Figure 6. Regions of the thorax phantom not included in the ROI represented in Figure 6 were cropped to prevent misrepresentation of the distortion levels in outer regions. Areas of agreement between both matrices are shown in grayscale, while distortion-caused discrepancies are highlighted in green and purple. Within the areas of discrepancy, the green highlighted areas are used to represent the original thorax model, the purple areas the distorted model. Colored areas at the outer edges are due to the selected region of interest, which discards areas with poor signal and increased artefact level, as detailed in the methods section. The outline of the mask used for the cropping is shown in red for both the sGRE and bSSFP deformation simulations.

FIGURE 6

Table 2 lists the RMS deformation values encountered in the area of the thoracic diaphragm for the sGRE and bSSFP sequence originating from the application of the spatial distortion model. The sum of all experimentally determined deformations is listed, as well as the contribution of the gradient or B_{0x} and susceptibility effects in *x*-direction. Additionally the simulated susceptibility-caused deformations in *z*-direction are shown for a gradient strength of $9\frac{\mathrm{mT}}{\mathrm{m}}$ and of $17\frac{\mathrm{mT}}{\mathrm{m}}$ for the sGRE and bSSFP sequence, respectively.

TABLE 2

Figure 7 shows the simulated patient-specific phantoms including spatial distortion effects, where changes in image quality due to the selected SNR level can be appreciated.

FIGURE 7

4. Discussion

Based on MR image analysis and numerical simulations, all major contributions to MR image distortions – B_0 inhomogeneities, gradient and susceptibility effects – were characterized. This provided the required quantifications to include a spatial distortion model in the CoMBAT phantom, which is the first computational phantom for MRgRT to model MR image distortions.

4.1. Phantom construction and quality assessment

Spatial distortion measurements were carried out relying on a custom-developed geometrical phantom. The phantom design included 4 modules that can be used as single units or assembled in a large structure depending on the available field of view. Preliminary measurements on single grid units revealed a manufacturing accuracy within 0.2 mm in plane and 0.5 mm in depth, including possible thickness variations and bending effects. Such an accuracy is compatible with the spatial resolution commonly used in CT and MR imaging, where the pixel spacing is around 1 mm and the slice thickness is in the order of 1-5 mm (for 2D MRI acquisitions). The CT analysis essentially confirmed the reliability of the custom phantom, also when

considering the intrinsic uncertainties in registering the CT/MR image to the virtual phantom model. The comparison of the convolved landmarks and the warped landmarks in the CT image registration step yielded a RMSD of 1.0 mm. This error was scaled according to the MR image voxel size lengths, assuming a 1 voxel error in the worst-case scenario: this resulted in a 1.2 mm error in the *x*- and *y*-direction. Since the deformation patterns in the *z*-direction were identical for the conventional and the reversed gradient image, the pointwise differences between the deformations were used as an error along *z*. It is worth stressing that errors in the *z*-direction were severely affected by the lower resolution (5-mm slice thickness) and by the selected distortion correction algorithm (2D vs. 3D), as discussed later.

The magnitude of spatial distortions due to the use of the geometrical phantom for measurements was specifically evaluated, relying on the same susceptibility simulation algorithm used for the CoMBAT phantom (32). A simulation was run at 1.5 T considering the presence of the PMMA phantom on the table support, including a thin layer of silica glue that was used to close the upper side of each phantom unit. Results show that average susceptibility-induced variations in the static magnetic field are in the micro-Tesla range, with corresponding deformations of -0.1±0.3 mm in the *z*-direction at the minimum gradient strength of 9 mT/m, corresponding to the sGRE sequence. Such deformations caused by susceptibility of the PMMA distortion phantom can be therefore considered negligible: they were ignored when separating the contribution of the CoMBAT phantom susceptibility and the effects due to the inhomogeneities of the static magnetic field.

4.2. Deformation fields of MR images

A conventional wide-bore 1.5 T MRI scanner was used for the determination of spatial distortions in MRgRT. The 1.5 T scanner served as a model for MR-linac systems in MRgRT, which have static magnetic field strengths between 0.35 T and 1.5 T (4). As high-speed image acquisition is a key requirement in extra-cranial sites, where breathing motion is predominant, two fast sequences (sGRE and bSSFP sequence) were chosen for image acquisition. A comparison of both images showed that the sGRE image, although showing a higher contrast, was much noisier than the bSSFP image. In order to improve the image quality for the image registration, the average of four acquisition was taken for each slice (Table 1). This corresponds to an increased image acquisition time and makes our specific implementation of the sGRE sequence less suitable

for radiation treatment than the bSSFP sequence, if structures with relaxation times similar to those of the phantom are imaged.

The quality of the registration between the acquired MR images and the virtual phantom was checked visually, following the quantitative validation performed on CT at 1 mm slice thickness. No major discrepancies were noticed in the MR image registration, despite the intrinsic coarser resolution in the *z*-direction (5 mm). The virtual phantom was rescaled accordingly to facilitate the registration process, and the implemented regularization options provided a sufficiently smooth deformation field to quantify distortion. The deformation behavior of the sGRE and bSSFP images is shown in Figure 5. As mentioned earlier, all plots in the upper and central panels show error bars which are overestimating the actual error, since they were calculated for the three-dimensional vector, instead of the *x*-component alone. The reversed-gradient method applied in the *x*-direction confirmed that the deformations caused by gradient nonlinearities are more severe than those caused by static B_0 and susceptibility differences, as already reported in the literature (31). The gradient-caused deformations reached values up to 3 mm, whereas the B_0 and susceptibility effects for the phantom mainly stayed below 1 mm.

In the slice-selection direction with a slice thickness of 5 mm, the deformation levels were largest, as was to be expected. Both the sGRE and the bSSFP image show a sign change of the deformations between grid 5 and 6, which are the grids before and after the B_0 isocenter. However the deformation magnitude and pattern differ substantially between both sequences. Maximum deformations of 3 mm at the outermost grids were registered for the sGRE sequence, whereas the bSSFP sequence reaches the 10 mm boundary. Additionally, the bSSFP sequence also exhibits a variable deformation pattern within each grid, with larger values for landmarks located at the borders of the grid. Additionally, it is know that the 2D distortion correction does not correct the distortions in *z*-direction (40). Since the 3D distortion correction was not available for the bSSFP sequence, this significantly contributed to the higher deformation levels compared to the sGRE sequence.

The performed statistical analysis confirmed that the spatial distortion measured for the two sequences is different in *x*- and *y*-direction, when checking the magnitude at corresponding locations within the distortion phantom. Although the difference was statistically significant, it should be noticed that the difference in the two sequences is on average within the expected error range in the analysis, i.e. below the voxel resolution (Figure 5, upper and central panels). The analysis along *z* was strongly affected by the larger deformation

values and the symmetric behavior when moving away from the center of the FOV (Figure 5, lower panels). This resulted in a non statistically significant difference overall, when considering all landmarks altogether. However, when analyzing the specific difference at variable *z*-location (individual grids), the distortion patterns for grids located away from the center of the FOV were proven to be different.

Since a study with absolutely identical imaging parameters could not be found in the literature, a comparison to literature values with best matching parameters is made here for completeness. In our measurements the maximum radial distance from the isocenter was around 255 mm. The range of our in-plane deformations is smaller than the deformation range of 0.00– 4.62 mm reported for a spin echo sequence at a radial distance of 250 mm elsewhere for a 1.5 T system (29), which, however, was not corrected for distortion.

4.3. Implementation in the CoMBAT phantom

The quantified deformations were embedded into the CoMBAT phantom, aiming at the availability of an anthropomorphic computational 4D CT/MRI phantom where MR-induced deformations can be modelled, and its effects quantified in dosimetric studies. The measured spatial distortion fields, considered as a whole or separated into distinct contributions, were included in the CoMBAT phantom, by deforming the ideal anatomy in the image space accordingly (Figure 6). Such an approach was motivated by the intrinsic features of the CoMBAT phantom, where anatomical changes due to breathing are defined in the image space, at adjustable spatial and temporal resolution. The vector field representing MR spatial distortion is fixed in absolute coordinates, but its application varies according to anatomical motion in the 4D MRI. Also, the specific contribution due to tissue susceptibility changes, as this is simulated according to each of the breathing phases in the 4D MRI. As a result, the decomposition of deformation effects does vary in the 4D dataset.

Table 2 lists the RMS distortion values discovered in the region of the thoracic diaphragm. Consistently with overall results in the area of interest (Figure 5), the corresponding deformation was significantly larger in z-direction (2.4 mm RMS for sGRE vs. less than 1 mm in *x* and *y*). In a similar fashion, the deformation in the diaphragm region was highly influenced by the implemented distortion correction method (3D vs. 2D), with an increase up to 5.3 mm RMS for the bSSFP sequence. As shown for comparison in Table 2, the contribution of the CoMBAT phantom susceptibility in *z*-direction was almost a factor of 2 higher for the sGRE sequence

(0.9 mm vs. 0.5 mm for bSSFP), in reason of the smaller slice selection gradient ($9\frac{\mathrm{mT}}{\mathrm{m}}$ vs. $17\frac{\mathrm{mT}}{\mathrm{m}}$). The susceptibility effects were attributable almost exclusively to the diamagnetic tissues, leading to a decrease of the overall magnetic field and a negative bias (32). Overall, the implementation of the deformations into the CoMBAT phantom showed that deformations levels at the thoracic diaphragm can reach values up to 5 mm in fast MR sequences lacking 3D distortion correction. These effects can be effectively minimized by changing the MRI acquisition plane from axial to either sagittal or coronal, where the main motion direction (superior-inferior) can be sampled at better resolution and reduced distortion levels. Such a technique is the current approach for motion management in MRgRT, which relies on respiratory gating triggered by a 2D cine-MR image (41). In order to derive quantitative 3D information for MRgRT, the acquisition of interleaved orthogonal (sagittal/coronal) cine-MRI slices intersecting the target has been also proposed (42, 43), with recent development toward simultaneous acquisition (44).

The developed phantom can be also adapted to reproduce measured clinical data, thus providing more detailed simulations on a case by case basis. We have shown that the phantom can be adjusted to embed any measured tumor shape, and to reproduce the motion detected in clinical scans, i.e. from 2D cine-MRI (21). As the SNR of the reconstructed image can be adjusted in the reconstruction process, patient-specific phantoms can also be tuned to reproduce specific noise levels, as measured in clinical MR images. The intrinsic advantage of the phantom is that high quality co-registered images can be generated, thus allowing the possibility to investigate the sensitivity of motion management strategies to image quality.

4.4. Intended use of the phantom

The inclusion of MRI spatial distortion in the CoMBAT phantom provides a simulation environment where the effect of distortion can be analyzed in a realistic anatomical representation and where time-resolved ground truth volumes are present. The proposed computational phantom is therefore put forward for imaging simulations in extra-cranial MR-guided radiotherapy, where several options exist to obtain respiratory correlated (4D) or time-resolved imaging. These include both images mostly useful in treatment planning (4D MRI) and time-resolved MR images to be acquired for online guidance (6,22,23), where spatial distortions could affect motion quantification (5). Moreover, as the computational phantom includes ideally segmented anatomy, with perfect separation in different tissues (including smallest details such as lung vessels), the

simulation can effectively account for susceptibility effects. This can be hardly achieved in real patient data, where segmentation is time consuming, with inter/intra-observer variability and intrinsically subject to partial volume effects. The CoMBAT phantom could therefore allow dedicated in-silico studies with an accurate segmentation level, and thus provide further insights on optimal strategies to achieve motion compensation in extra-cranial MR-guided radiotherapy. As co-registered CT images are provided, the phantom can also serve as an experimental platform to perform dosimetric studies, independently of registration errors.

The quantification of spatial distortion for imaging sequences used in MR-guided radiotherapy may turn out to be useful also outside the envisioned computational phantom environment. Although susceptibility effects can be hardly simulated in clinical data using the proposed approach, system-related distortions (namely static magnetic field inhomogeneities and gradient effects) can be effectively accounted for. This is of particular interest for MRI-only radiotherapy (1), where the treatment planning CT is replaced by synthetic images generated from the clinical MR scans (45, 46). In this case, knowledge of the residual distortion in treatment planning images may be beneficial to analyze potential detrimental effects due to systematic uncertainties in the anatomical description.

As a general requirement, the distortion model is meant to represent an up-to-date situation in MR-guided radiotherapy. It has been shown recently that the behavior of gradient nonlinearities in a low field MR-linac can change substantially after major repair and re-shimming (47), which would require an update of the distortion model before it can be effectively used. Check of spatial distortions in MR-guided radiotherapy is an integral part for system commissioning and quality assurance (48-50). Therefore, spatial distortion models could be checked and updated frequently, counting on the availability of repeated measurements during clinical use of MR-guided systems. In case deviations are highlighted during quality assurance, the distortion model should be updated to account for the measured changes. The in-house developed distortion phantom has been proven to provide sufficient accuracy for such repeated checks.

4.5. Limitations and validity of reported results

In this study, we presented data acquisition and analysis procedures aiming at the quantification and modeling of spatial distortions, where individual contributions are separated. Major effects were considered,

namely static field inhomogeneities, gradient non linearities and tissue susceptibility effects. Inhomogeneities of the radio-frequency field, as well as the use of different coils, have not been specifically considered, although the CoMBAT phantom can potentially model the spatial profile of radio-frequency coils sensitivity, thus providing the methodological tool to address such effects. Also, potential errors due to eddy currents and rapidly changing gradients were not considered, although these might induce significant image artifacts (51). Likewise, the influence of specific immobilization devices has not been considered, as this would require modeling of the specific material properties in terms of magnetic susceptibility.

Spatial distortions were modeled as a deformation vector field, to be applied to the synthetic images generated by the CoMBAT phantom. The vector field was calculated relying on DIR, as an alternative to selecting and matching corresponding phantom landmarks. Such a choice provided an automated procedure to avoid time consuming landmark detection, that would have been necessary considering the non-uniform intensities across the acquired MR images. The chosen DIR implementation via regularized B-spline and Morphons algorithms ensured sufficient regularity in the calculated vector field, as confirmed by the Jacobian determinant quantification (52). On the other hand, the DIR-based approach required the verification of landmark matching via visual inspection, due to the challenges in implementing an automated procedure. As suggested in a recent review work, a case specific evaluation for the verification of DIR performance is always recommended, with quantitative measures to be favored over qualitative checks (53).

Distortions were applied via the calculated vector fields to each of the breathing phases following 4D image reconstruction. The main limitation of this approach is that motion of spins during MR image acquisition is not specifically modeled, under the assumption that local distortion values are constant during acquisition. Considering the 300-500 ms acquisition time of a single 2D slice in the tested sequences, the assumption is indeed valid around end-expiration, where the breathing dynamics is expected to be slower. Conversely, more significant effects can be expected around inspiration, where the generated phantom images may fail to account for motion blur artefacts. The spatial distortions model developed in this work could be also used in alternative phantom formulations where Bloch equations are used, as a way to define motion during MR acquisition of a given voxel sample. This would provide a way to account for motion during acquisition, as the effect is expected to be dependent on motion magnitude, which is different at distinct voxel location.

Our current work focused on the simulation of 2D MR image acquisition, by selecting the sGRE and bSSFP sequences that are currently modeled in the CoMBAT phantom (22). The clinical use of 2D sequences is well

established for motion management in MRI guided radiotherapy, especially for 2D bSSFP (54-56). The use of 3D sequences for guidance is currently limited to static 3D sGRE, 3D bSSFP (57) and 3D T1 weighted FFE (Fast Field Echo) (58). The spatial distortion model presented in this work can therefore be used to analyze distortion in 2D cine imaging for guidance and in 4D MRI images reconstructed via slice stacking. There is indeed and increasing interest toward 3D sequences with non-Cartesian k-space sampling (5, 6), aiming at reduced artefacts in 4D MRI reconstruction. Although those sequences are not modeled in the current CoMBAT implementation, this can be extended as future work, as facilitated by the intrinsic isotropic phantom resolution (1 x 1 x 1 mm^3).

The analysis was limited to axial slices, with effective separation of static field inhomogeneities, gradient, and susceptibility-related effects feasible only in the *x*-direction. The choice of the axial orientation is justified by the intrinsic features of MR-linac design, that determines higher uncertainties in the magnetic field homogeneities (59). In further studies, the analysis could be repeated by switching the phase and frequency-encoding directions, to achieve the separation of different contributions in the axial plane, and by changing the gradient polarity also along *z*. As discussed previously, MR image acquisition can be extended to other anatomical orientations, with a further possibility to implement 3D acquisition modalities where two phase-encoding directions are used for k-space sampling. As combinations are manifold, an extensive analysis is hardly applicable, although the methods shown here can be used for arbitrary orientation modalities and with alternative MR sequences as well. The custom-developed distortion phantom was designed so that modules can be arranged in any orientation, thus providing a useful phantom to test the three main anatomical orientations (i.e. axial, sagittal, and coronal). The limitation in this case is given by the intrinsic phantom accuracy in the direction orthogonal to the laser-cut grids, which is lower than in the grid plane. Also, oblique planes could be hardly tested, and they would require a rotational symmetric arrangement of grid points, that cannot be achieved with the current phantom.

A key component in separating the different contributions of spatial distortions is the reversed-gradient method which was applied to MR images after the vendor-supplied distortion correction was used. This was motivated by the assumption that the distortion correction would always be applied in MRgRT clinical practice to guarantee maximum geometrical accuracy. A deformation evaluation without the distortion correction would thus exaggerate the quantified deformation levels. It should be noted that distortion correction methods implemented in commercial MRI scanners typically correct for local changes in the

magnetic field strength, relying on device-specific information to map the combined effects of B_0 inhomogeneities and gradient nonlinearities (40). It has been shown that these effects are mostly dependent on the position inside the scanner field of view, with larger impact at the border. It is fair to assume that the applied corrections are symmetric with respect to gradient polarity, as corrections are meant to compensate for the local field inaccuracies. We therefore believe that this does not hinder application of the reversed-gradient method to distortion-corrected images. As the gradient-induced distortions patterns agree nicely with the expectations, with larger effects toward the borders of the field of view, we considered this assumption to be confirmed.

5. Conclusion

In this work, we performed a detailed spatial deformation analysis consisting of experimental values for a conventional 1.5 T MRI scanner, complemented by numerical simulations. We were able to derive a quantitative model of spatial distortions, and to integrate it for the first time into a computational 4D anthropomorphic MRI phantom to be used in simulations studies. Pronounced differences in the deformation levels between two different pulse sequences showed that sequences have to be modeled individually, as not only the used gradient strengths but also the switching scheme and available distortion correction algorithms have major effects on the deformation patterns and magnitude. Future work will extend the modeled MR imaging sequences to consider variable slice orientation and different field strengths. The methodological tools developed in this work will therefore provide the ability to analyze advanced k-space sampling methods in time-resolved MR-guided radiotherapy.

References

1. Owrangi AM, Greer PB, Glide-Hurst CK. MRI-only treatment planning: benefits and challenges. Phys Med Biol. 2018;63(5):05TR1.

2. Corradini S, Alongi F, Andratschke N, Belka C, Boldrini L, Cellini F, et al. MR-guidance in clinical reality: current treatment challenges and future perspectives. Radiat Oncol. 2019;14(1):92.

3. Jones KM, Michel KA, Bankson JA, Fuller CD, Klopp AH, Venkatesan AM. Emerging Magnetic Resonance Imaging Technologies for Radiation Therapy Planning and Response Assessment. Int J Radiat Oncol Biol Phys. 2018;101(5):1046-56.

4. Liney GP, Whelan B, Oborn B, Barton M, Keall P. MRI-Linear Accelerator Radiotherapy Systems. Clin Oncol (R Coll Radiol). 2018;30(11):686-91.

5. Paganelli C, Whelan B, Peroni M, Summers P, Fast M, van de Lindt T, et al. MRI-guidance for motion management in external beam radiotherapy: current status and future challenges. Phys Med Biol. 2018;63(22):22TR03.

6. Stemkens B, Paulson ES, Tijssen RHN. Nuts and bolts of 4D-MRI for radiotherapy. Phys Med Biol. 2018;63(21):21TR01.

7. Kauczor HU, Plathow C. Imaging tumour motion for radiotherapy planning using MRI. Cancer Imaging. 2006;6:S140-4.

8. Menten MJ, Wetscherek A, Fast MF. MRI-guided lung SBRT: Present and future developments. Phys Med. 2017;44:139-49.

9. Crijns SP, Kok JG, Lagendijk JJ, Raaymakers BW. Towards MRI-guided linear accelerator control: gating on an MRI accelerator. Phys Med Biol. 2011;56(15):4815-25.

10. Hunt A, Hansen VN, Oelfke U, Nill S, Hafeez S. Adaptive Radiotherapy Enabled by MRI Guidance. Clin Oncol (R Coll Radiol). 2018;30(11):711-9.

11. Kontaxis C, Bol GH, Stemkens B, Glitzner M, Prins FM, Kerkmeijer LGW, et al. Towards fast online intrafraction replanning for free-breathing stereotactic body radiation therapy with the MR-linac. Phys Med Biol. 2017;62(18):7233-48.

12. Biederer J, Dinkel J, Remmert G, Jetter S, Nill S, Moser T, et al. 4D-Imaging of the lung: reproducibility of lesion size and displacement on helical CT, MRI, and cone beam CT in a ventilated ex vivo system. Int J Radiat Oncol Biol Phys. 2009;73(3):919-26.

13. Biederer J, Plathow C, Schoebinger M, Tetzlaff R, Puderbach M, Bolte H, et al. Reproducible Simulation of Respiratory Motion in Porcine Lung Explants. Rofo. 2006;178(11):1067-72.

14. Mann P, Witte M, Moser T, Lang C, Runz A, Johnen W, et al. 3D dosimetric validation of motion compensation concepts in radiotherapy using an anthropomorphic dynamic lung phantom. Phys Med Biol. 2017;62(2):573-95.

15. Bolwin K, Czekalla B, Frohwein LJ, Buther F, Schafers KP. Anthropomorphic thorax phantom for cardio-respiratory motion simulation in tomographic imaging. Phys Med Biol. 2018;63(3):035009.

16. Perrin RL, Zakova M, Peroni M, Bernatowicz K, Bikis C, Knopf AK, et al. An anthropomorphic breathing phantom of the thorax for testing new motion mitigation techniques for pencil beam scanning proton therapy. Phys Med Biol. 2017;62(6):2486-504.

17. Neufeld E, Lloyd B, Schneider B, Kainz W, Kuster N. Functionalized Anatomical Models for Computational Life Sciences. Front Physiol. 2018;9:1594.

18. Xu XG. An exponential growth of computational phantom research in radiation protection, imaging, and radiotherapy: a review of the fifty-year history. Phys Med Biol. 2014;59(18):R233-302.

19. Kainz W, Neufeld E, Bolch WE, Graff CG, Kim CH, Kuster N, et al. Advances in Computational Human Phantoms and Their Applications in Biomedical Engineering - A Topical Review. IEEE Trans Radiat Plasma Med Sci. 2019;3(1):1-23.

20. Paganelli C, Kipritidis J, Lee D, Baroni G, Keall P, Riboldi M. Image-based retrospective 4D MRI in external beam radiotherapy: A comparative study with a digital phantom. Med Phys. 2018;45(7):3161-72.

21. Paganelli C, Portoso S, Garau N, Meschini G, Via R, Buizza G, et al. Time-resolved volumetric MRI in MRI-guided radiotherapy: an in silico comparative analysis. Phys Med Biol. 2019;64(18):185013.

22. Paganelli C, Summers P, Gianoli C, Bellomi M, Baroni G, Riboldi M. A tool for validating MRI-guided strategies: a digital breathing CT/MRI phantom of the abdominal site. Med Biol Eng Comput. 2017;55(11):2001-14.

23. Huang SY, Seethamraju RT, Patel P, Hahn PF, Kirsch JE, Guimaraes AR. Body MR Imaging: Artifacts, k-Space, and Solutions. Radiographics. 2015;35(5):1439-60.

24. Segars WP, Sturgeon G, Mendonca S, Grimes J, Tsui BM. 4D XCAT phantom for multimodality imaging research. Med Phys. 2010;37(9):4902-15.

25. Lowther N, Ipsen S, Marsh S, Blanck O, Keall P. Investigation of the XCAT phantom as a validation tool in cardiac MRI tracking algorithms. Phys Med. 2018;45:44-51.

26. Wissmann L, Santelli C, Segars WP, Kozerke S. MRXCAT: Realistic numerical phantoms for cardiovascular magnetic resonance. J Cardiovasc Magn Reson. 2014;16:63.

27. Lo WC, Chen Y, Jiang Y, Hamilton J, Grimm R, Griswold M, et al. Realistic 4D MRI abdominal phantom for the evaluation and comparison of acquisition and reconstruction techniques. Magn Reson Med. 2019;81(3):1863-75.

28. Mattila S, Renvall V, Hiltunen J, Kirven D, Sepponen R, Hari R, et al. Phantom-based evaluation of geometric distortions in functional magnetic resonance and diffusion tensor imaging. Magn Reson Med. 2007;57(4):754-63.

29. Torfeh T, Hammoud R, Perkins G, McGarry M, Aouadi S, Celik A, et al. Characterization of 3D geometric distortion of magnetic resonance imaging scanners commissioned for radiation therapy planning. Magn Reson Imaging. 2016;34(5):645-53.

30. Sumanaweera T, Glover G, Song S, Adler J, Napel S. Quantifying MRI geometric distortion in tissue. Magn Reson Med. 1994;31(1):40-7.

31. Stanescu T, Jaffray D. Investigation of the 4D composite MR image distortion field associated with tumor motion for MR-guided radiotherapy. Med Phys. 2016;43(3):1550-62.

32. Kroll C, Dietrich, O; Bortfeldt, J; Paganelli, C; Baroni, G; Kamp, F; Neppl, S; Belka, C; Parodi, K; Riboldi, M. Improving the modelling of susceptibility-induced spatial distortions in MRI-guided extra-cranial radiotherapy. Phys Med Biol. 2019;64(20):9.

33. Fedorov A, Beichel R, Kalpathy-Cramer J, Finet J, Fillion-Robin JC, Pujol S, et al. 3D Slicer as an image computing platform for the Quantitative Imaging Network. Magn Reson Imaging. 2012;30(9):1323-41.

34. Shackleford JA, Kandasamy N, Sharp GC. On developing B-spline registration algorithms for multi-core processors. Phys Med Biol. 2010;55(21):6329-51.

35. Janssens G, Jacques L, Orban de Xivry J, Geets X, Macq B. Diffeomorphic registration of images with variable contrast enhancement. Int J Biomed Imaging. 2011;2011:891585.

36. Bakker CJ, Moerland MA, Bhagwandien R, Beersma R. Analysis of machine-dependent and object-induced geometric distortion in 2DFT MR imaging. Magn Reson Imaging. 1992;10(4):597-608.

37. Baldwin LN, Wachowicz K, Thomas SD, Rivest R, Fallone BG. Characterization, prediction, and correction of geometric distortion in 3 T MR images. Med Phys. 2007;34(2):388-99.

38. Tadic T, Jaffray DA, Stanescu T. Harmonic analysis for the characterization and correction of geometric distortion in MRI. Med Phys. 2014;41(11):112303.

39. Ji JX, B. SJ, Rane SD. PULSAR: A Matlab toolbox for parallel magnetic resonance imaging using array coils and multiple channel receivers. Concepts in Magnetic Resonance Part B: Magnetic Resonance Engineering 31B. 2007:13.
40. Karger CP, Hoss A, Bendl R, Canda V, Schad L. Accuracy of device-specific 2D and 3D image distortion correction algorithms for magnetic resonance imaging of the head provided by a manufacturer. Phys Med Biol. 2006;51(12):N253-61.
41. Heerkens HD, van Vulpen M, van den Berg CA, Tijssen RH, Crijns SP, Molenaar IQ, et al. MRI-based tumor motion characterization and gating schemes for radiation therapy of pancreatic cancer. Radiother Oncol. 2014;111(2):252-7.
42. Bjerre T, Crijns S, af Rosenschold PM, Aznar M, Specht L, Larsen R, et al. Three-dimensional MRI-linac intra-fraction guidance using multiple orthogonal cine-MRI planes. Phys Med Biol. 2013;58(14):4943-50.
43. Stemkens B, Tijssen RH, de Senneville BD, Lagendijk JJ, van den Berg CA. Image-driven, model-based 3D abdominal motion estimation for MR-guided radiotherapy. Phys Med Biol. 2016;61(14):5335-55.
44. Mickevicius NJ, Paulson ES. Simultaneous orthogonal plane cine imaging with balanced steady-state free-precession contrast using k-t GRAPPA. Phys Med Biol. 2018;63(15):15NT02.
45. Edmund JM, Nyholm T. A review of substitute CT generation for MRI-only radiation therapy. Radiat Oncol. 2017;12(1):28.
46. Johnstone E, Wyatt JJ, Henry AM, Short SC, Sebag-Montefiore D, Murray L, et al. Systematic Review of Synthetic Computed Tomography Generation Methodologies for Use in Magnetic Resonance Imaging-Only Radiation Therapy. Int J Radiat Oncol Biol Phys. 2018;100(1):199-217.
47. Nejad-Davarani SP, Kim JP, Du D, Glide-Hurst C. Large field of view distortion assessment in a low-field MR-linac. Med Phys. 2019;46(5):2347-55.
48. Keesman R, van de Lindt TN, Juan-Cruz C, van den Wollenberg W, van der Bijl E, Nowee ME, et al. Correcting geometric image distortions in slice-based 4D-MRI on the MR-linac. Med Phys. 2019;46(7):3044-54.
49. Michael Gach H, Curcuru AN, Wittland EJ, Maraghechi B, Cai B, Mutic S, et al. MRI quality control for low-field MR-IGRT systems: Lessons learned. J Appl Clin Med Phys. 2019;20(10):53-66.
50. Tijssen RHN, Philippens MEP, Paulson ES, Glitzner M, Chugh B, Wetscherek A, et al. MRI commissioning of 1.5T MR-linac systems - a multi-institutional study. Radiother Oncol. 2019;132:114-20.

51. Lee HS, Choi SH, Park SH. Single and double acquisition strategies for compensation of artifacts from eddy current and transient oscillation in balanced steady-state free precession. Magn Reson Med. 2017;78(1):254-63.

52. Brock KK, Mutic S, McNutt TR, Li H, Kessler ML. Use of image registration and fusion algorithms and techniques in radiotherapy: Report of the AAPM Radiation Therapy Committee Task Group No. 132. Med Phys. 2017;44(7):e43-e76.

53. Paganelli C, Meschini G, Molinelli S, Riboldi M, Baroni G. "Patient-specific validation of deformable image registration in radiation therapy: Overview and caveats". Med Phys. 2018;45(10):e908-e22.

54. Finazzi T, Palacios MA, Haasbeek CJA, Admiraal MA, Spoelstra FOB, Bruynzeel AME, et al. Stereotactic MR-guided adaptive radiation therapy for peripheral lung tumors. Radiother Oncol. 2019;144:46-52.

55. Henke LE, Contreras JA, Green OL, Cai B, Kim H, Roach MC, et al. Magnetic Resonance Image-Guided Radiotherapy (MRIgRT): A 4.5-Year Clinical Experience. Clin Oncol (R Coll Radiol). 2018;30(11):720-7.

56. van Sornsen de Koste JR, Palacios MA, Bruynzeel AME, Slotman BJ, Senan S, Lagerwaard FJ. MR-guided Gated Stereotactic Radiation Therapy Delivery for Lung, Adrenal, and Pancreatic Tumors: A Geometric Analysis. Int J Radiat Oncol Biol Phys. 2018;102(4):858-66.

57. Raaymakers BW, Jurgenliemk-Schulz IM, Bol GH, Glitzner M, Kotte A, van Asselen B, et al. First patients treated with a 1.5 T MRI-Linac: clinical proof of concept of a high-precision, high-field MRI guided radiotherapy treatment. Phys Med Biol. 2017;62(23):L41-L50.

58. Werensteijn-Honingh AM, Kroon PS, Winkel D, Aalbers EM, van Asselen B, Bol GH, et al. Feasibility of stereotactic radiotherapy using a 1.5T MR-linac: Multi-fraction treatment of pelvic lymph node oligometastases. Radiother Oncol. 2019;134:50-4.

59. Jackson S, Glitzner M, Tijssen RHN, Raaymakers BW. MRI B 0 homogeneity and geometric distortion with continuous linac gantry rotation on an Elekta Unity MR-linac. Phys Med Biol. 2019;64(12):12NT01.

Figure legends

Figure 1. Diagram visualizing the workflow for the measurement and integration of spatial distortions in the CoMBAT phantom. On the left side, specific contributions from the current work are highlighted: parallelograms represent data, rectangles with thick lines are implemented procedures, and ovals represent output of such procedures. The susceptibility simulation algorithm reported in (32) provided the susceptibility distortion simulation in the CoMBAT phantom (thick arrow, right side) and the quantification of susceptibility effects in the physical distortion phantom (dashed arrows, right side) aiming at the separation of B_0 inhomogeneities distortion effects.

Figure 2. Construction sketch of the used distortion phantom built out of PMMA. The phantom with outer dimensions of (369 × 300 × 500) mm^3 consists of four individual modules which can be mutually aligned with the help of alignment nobs at arrow tips as shown on the left. Each module hosts five distortion grids with specified landmarks at grid intersections, as shown on the right. The distortions grids positioned in the phantom cover an area of (345 × 275) mm^2 over 480 mm in the third direction For contrast enhancement, the modules can be filled with water or contrast agent solutions.

Figure 3. Left panel: air bubbles in phantom. Right panel: setup for the air bubble removal developed for the phantoms, showing the vacuum chamber with the water filled phantom inside.

Figure 4. Axial (A, C) and coronal (B, D) slices of the spatial distortion phantom acquired with sGRE (upper panels) and bSSFP sequence (lower panels). The green point in all panels depicts the position of the imaging isocenter. The two central modules featured the lowest distortion levels, whereas the geometry in outer modules was significantly degraded, as clearly visible in panels B and D.

Figure 5. Results of the reversed-gradient approach for the bSSFP and sGRE and images with gradient polarity reversal in the frequency-encoding *x*-direction. The schematic in the lower left corner shows the four modules of the phantom, from which only the two central modules (grids 6 to 15 in dark gray) were used for the deformation analysis. The central and right panels show the residual deformation for grid points located in each grid, where red vertical lines separate the points within individual grids (sorted according to increasing Z, indicated by the red arrow "B" in the lower left panel). Within the grids, points are sorted column-wise according to their *x*-coordinate from left to right (indicated by the red arrows "A" in the lower left panel). Errors are overlaid in light blue. Errors for the $\boldsymbol{B_0}$ and susceptibility-caused residual deformations in *x*-

direction, and for gradient effects in *x*-direction are extrapolated from the CT image analysis. Errors for the $\boldsymbol{B_0}$, gradient and susceptibility residual deformations in the conventional and reversed gradient polarity image in *z*-direction (lower panels) are calculated as the difference. The upper left panel shows a zoom for the gradient effects in the 2 central grids for the bSSFP sequence, as indicated by the corresponding green box.

Figure 6. Overlay of original thorax phantom (green) and deformed thorax phantom (purple) using the deformation fields extracted from MR images: areas of agreement are shown in grayscale. The thorax phantoms are displayed using the same window, all differences in contrast are caused by the sequence used for image acquisition. Upper panels: sGRE sequence, lower panels: bSSFP sequence. Both sequences are shown at expiration (left hand side) and inspiration (right hand side). The dashed yellow line is shown to highlight motion of anatomical structures due to breathing (expiration vs. inspiration).

Figure 7. Coronal and sagittal cuts of the patient-specific phantoms P01 and P02, with the red cross centered in the tumor. For each of the two phantoms, images at exhale (left columns) and inhale (right columns) are shown at different SNR levels (20 vs. 2, in upper vs. lower panels).

Acknowledgements

This work was supported by the German Research Foundation (DFG) Cluster of Excellence Munich-Centre for Advanced Photonics (MAP). The construction of the used phantom was founded by the Maier-Leibnitz-Laboratorium (MLL), Garching. Special thanks to Klaus Wirgler for providing the construction plan of the distortion phantom. The OpenREGGUI collaboration is acknowledged for sharing REGGUI. Clarissa Kroll gratefully acknowledges a study scholarship by the Heinrich Böll Foundation. Jonathan Bortfeldt acknowledges support by the COFUND-FP-CERN-2014 program (grant 665779).

Conflict of interest statement

The Department of Radiation Oncology of the University Hospital at Ludwig-Maximilians University has research agreements with Brainlab, Elekta and Viewray.

Table 1. Sequence parameters for the sGRE and bSSFP sequence used for the MR image acquisition of the phantom.

Parameter	**2D sGRE**	**2D bSSFP**
Repetition time T_R (ms)	5.80	3.24
Echo time T_E (ms)	2.78	1.62
Flip angle	8°	68°
Receiver bandwidth (Hz/pixel)	295	590
Matrix size (in-plane interpolated)	384 × 264 × 100	384 × 264 × 100
Voxel size (mm³)	1.17 × 1.17 × 5.00	1.17 × 1.17 × 5.00
Field of view (mm³)	450 × 309 × 500	450 × 309 × 500
Slice orientation	axial	Axial
Slice selection gradient (mT/m)	9	17
Number of image averages	4	1
Phase sampling (resolution)	0.65	0.65
Acquisition time	4 × 0.4988 s/slice	0.3125 s/slice
Distortion correction mode	3D	2D

Table 2. Summary of RMS deformation values in the region of the thoracic diaphragm, as found for the sGRE and bSSFP sequence in a 1.5 T scanner. The term "combined" in the effect column stands for considering all causes of distortion. The contribution of susceptibility in the z-direction is also shown for comparison.

effect	**direction**	**sGRE [mm]**	**bSSFP [mm]**
combined	*x*	0.8	0.4
combined	*y*	1.0	0.5
combined	*z*	2.4	5.3
B_{0x} and χ_x	*x*	0.5	0.2
gradient G_x	*x*	0.6	0.5
$\chi_{z,1.5\,T}$	*z*	0.9	0.5

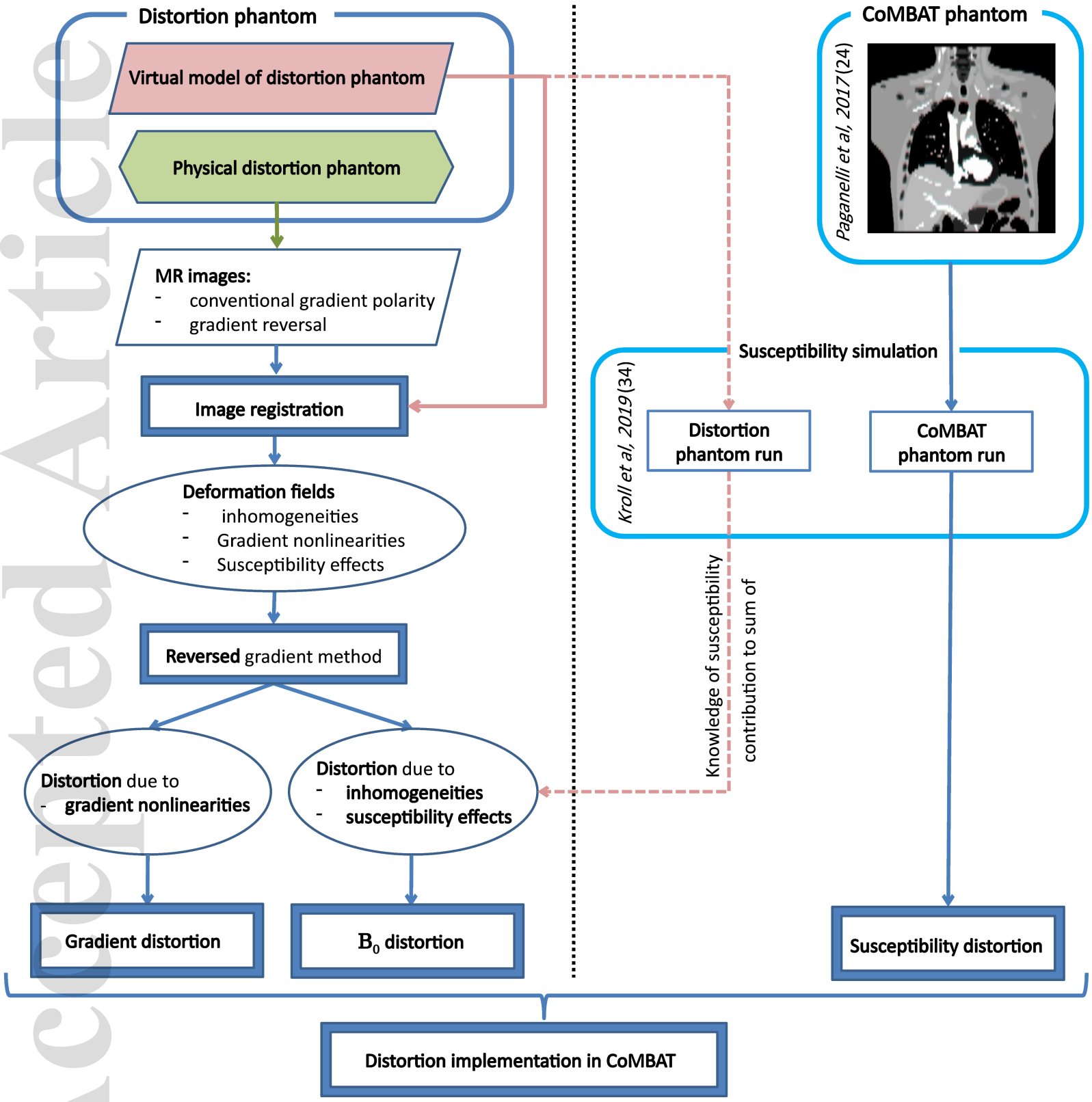

mp_14611_f1.eps

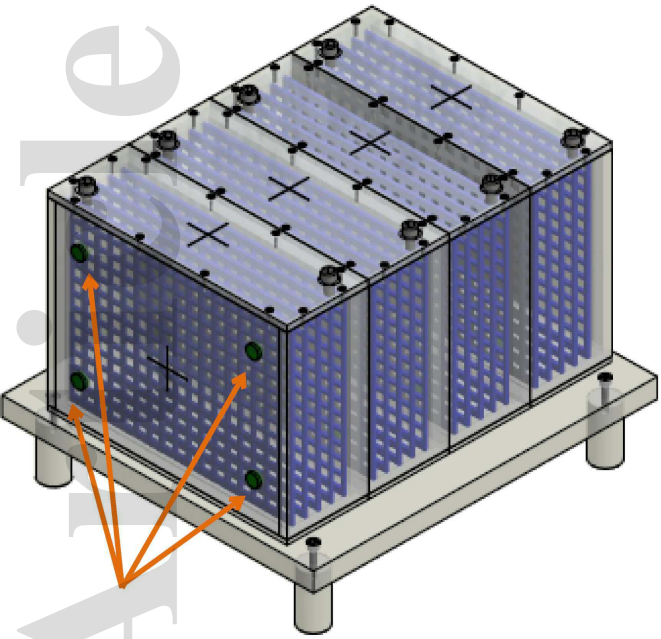

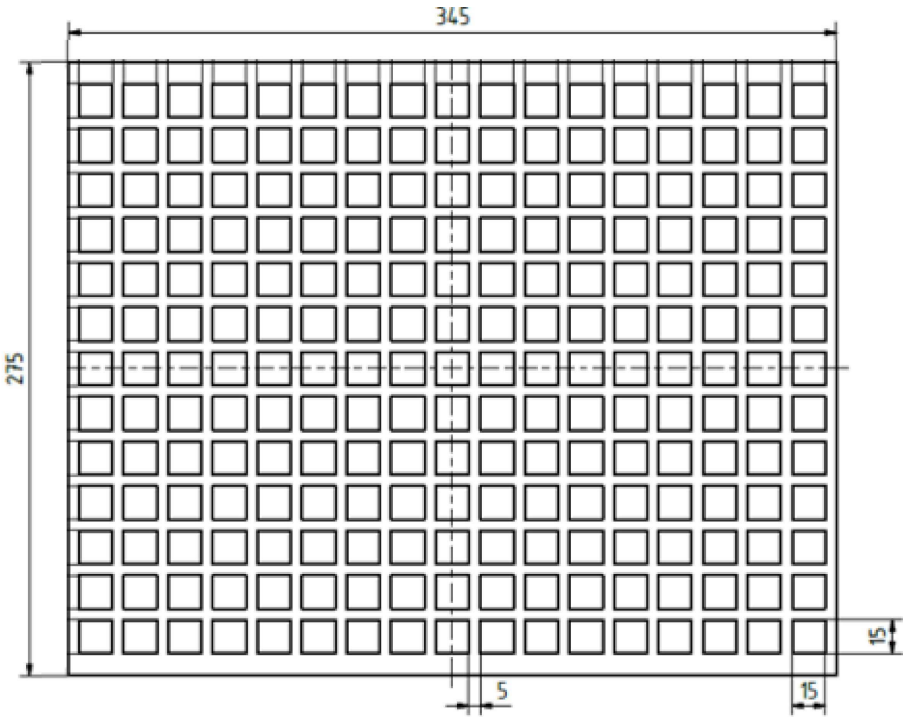

mp_14611_f2.eps

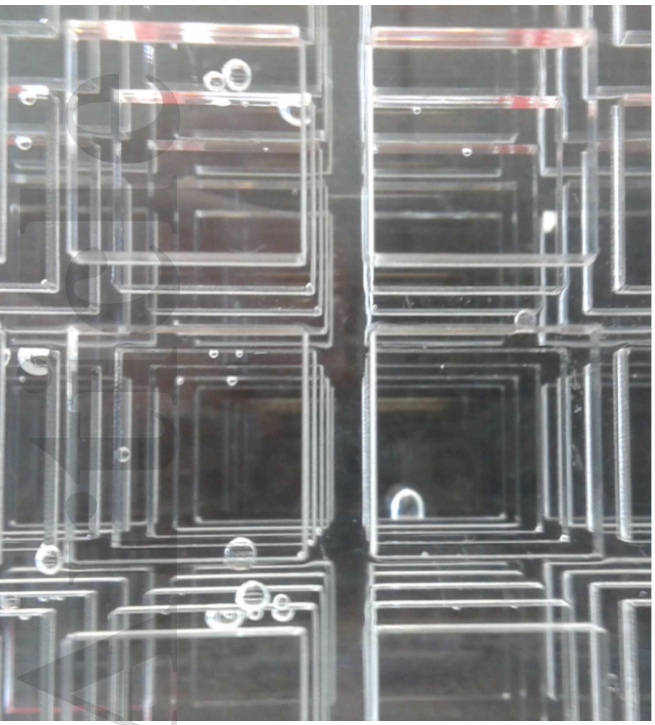

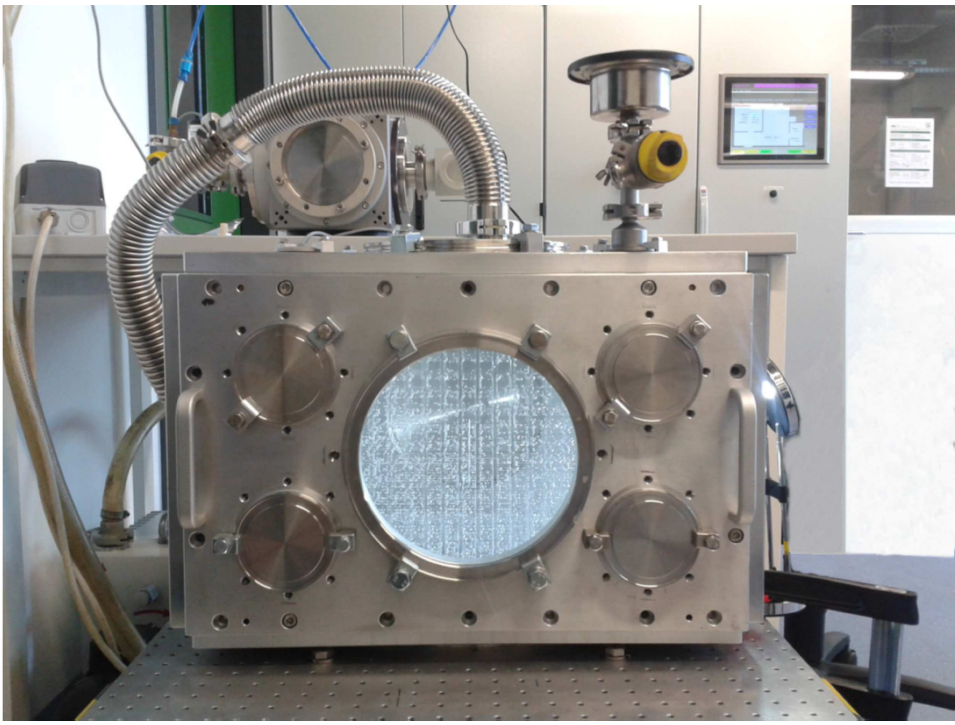

mp_14611_f3.eps

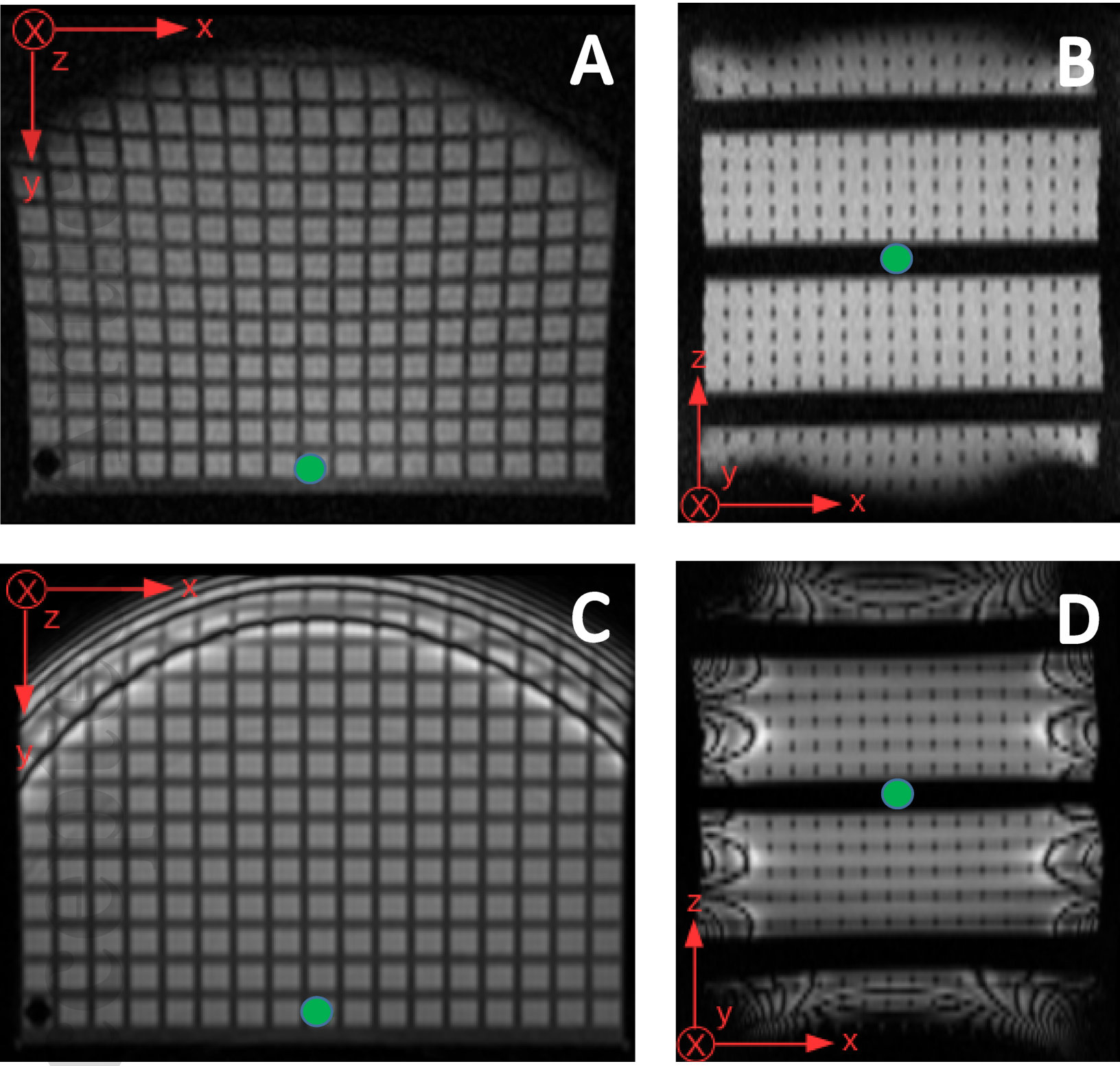

mp_14611_f4.eps

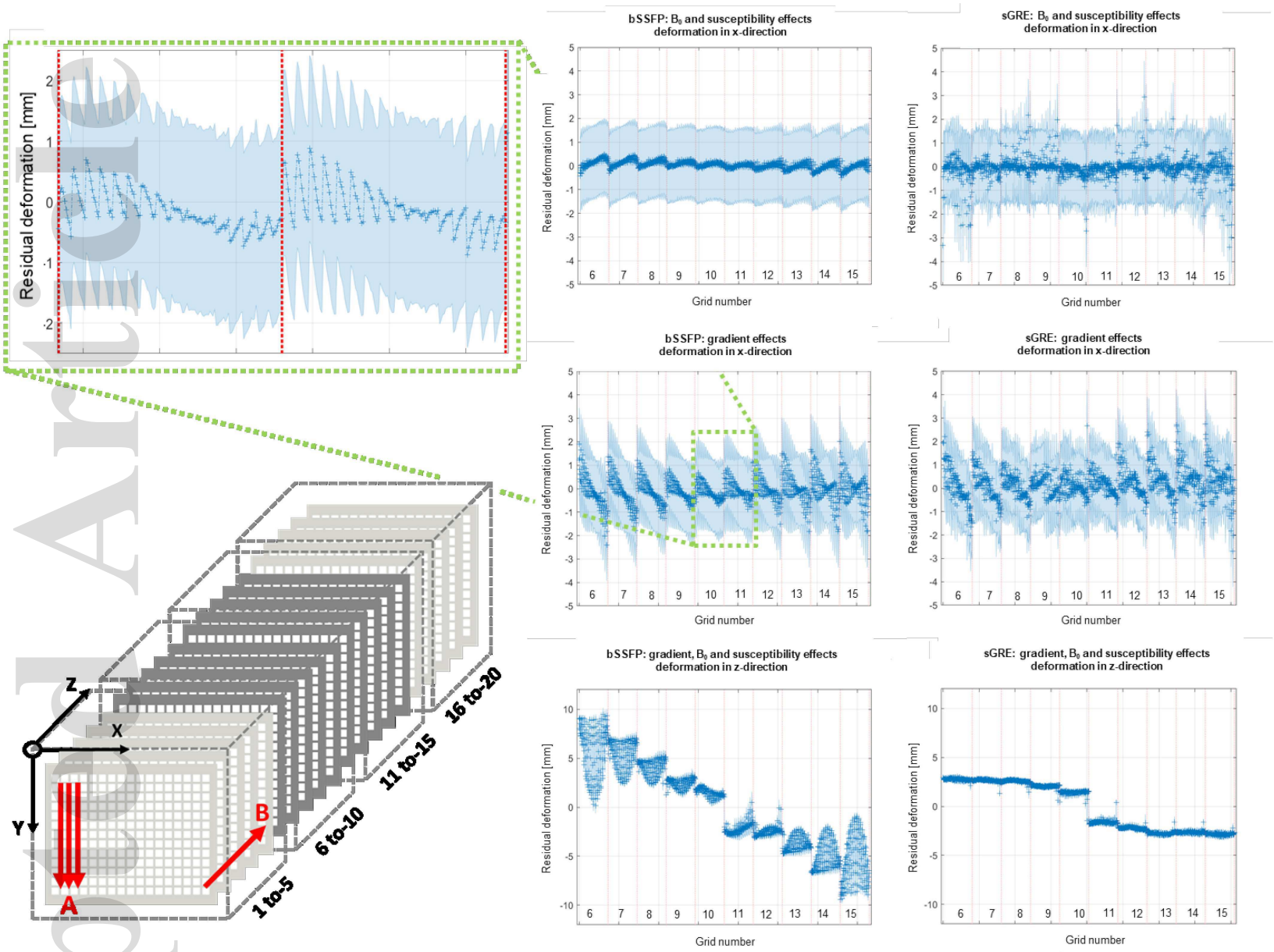

mp_14611_f5.eps

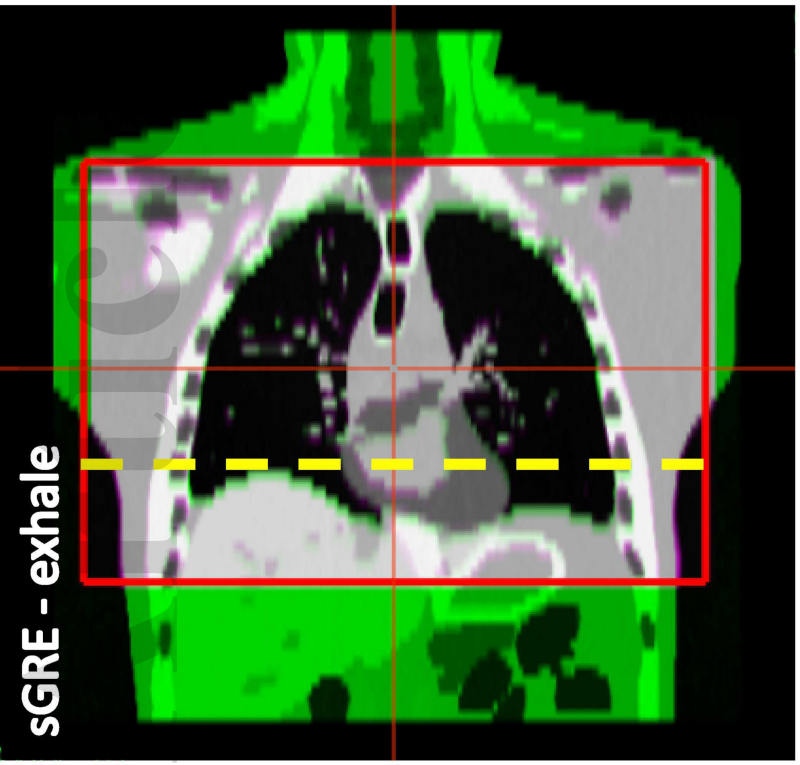

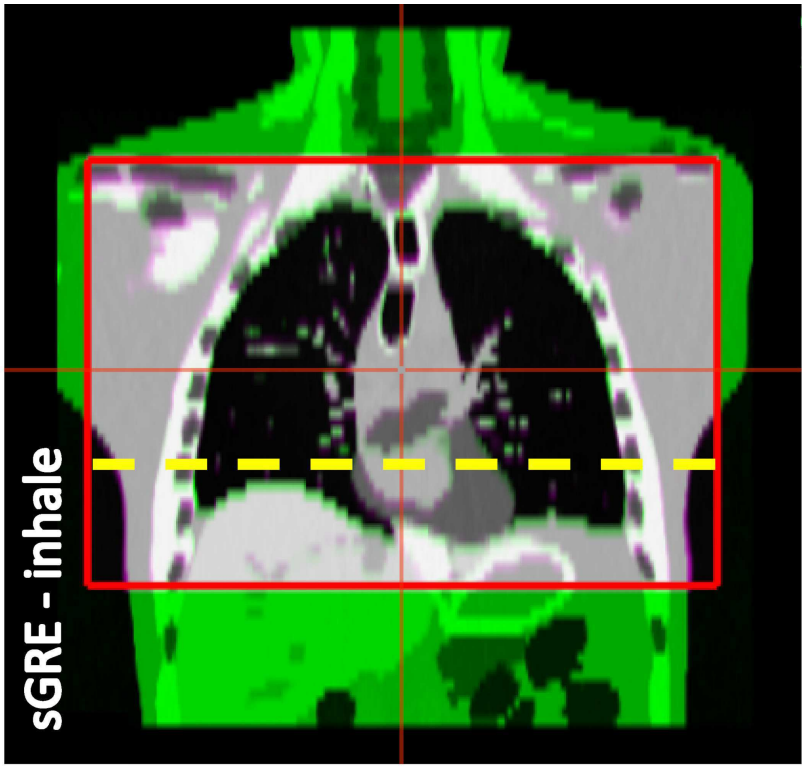

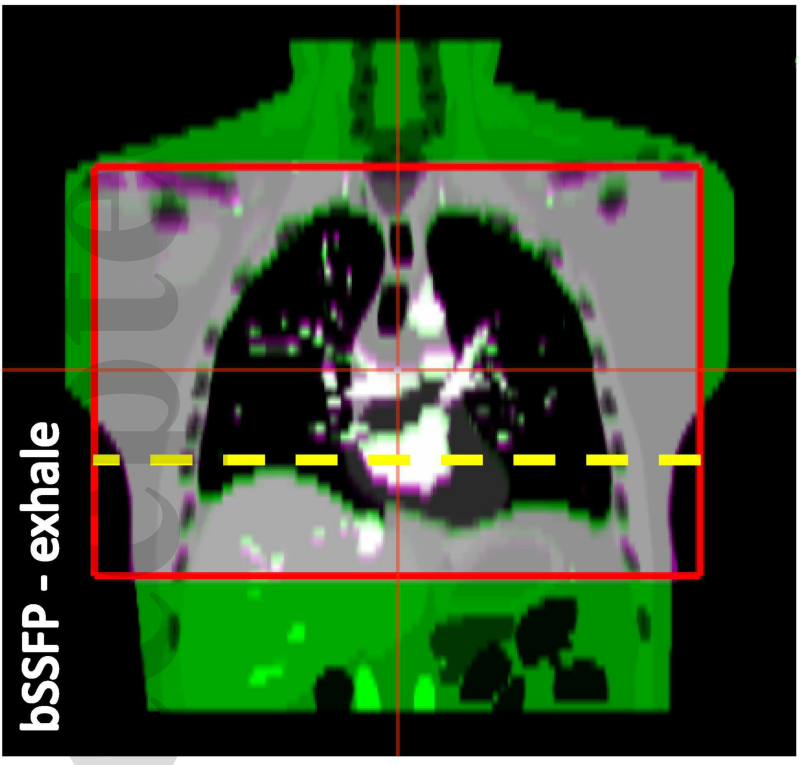

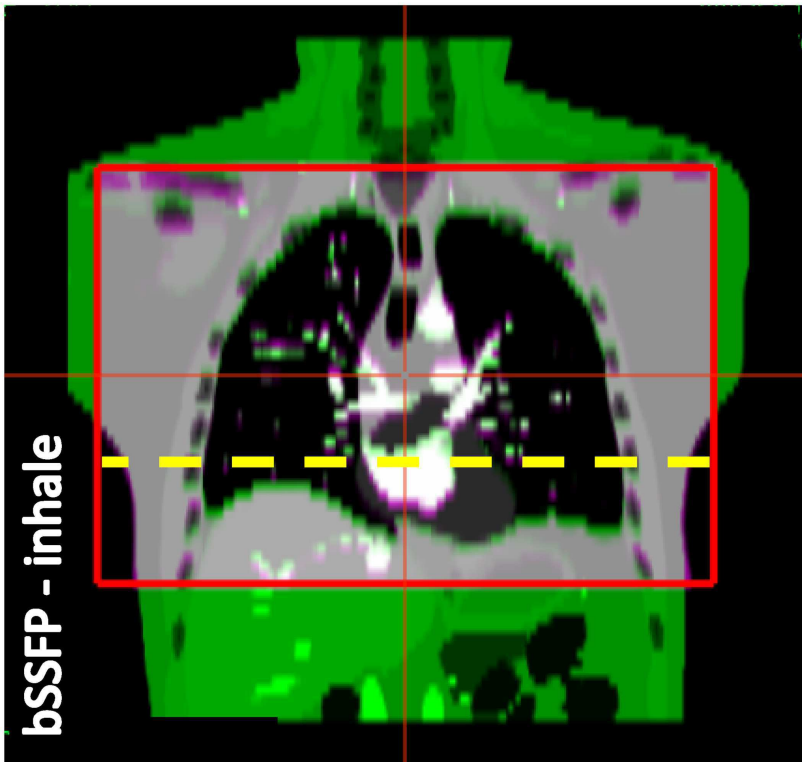

mp_14611_f6.eps

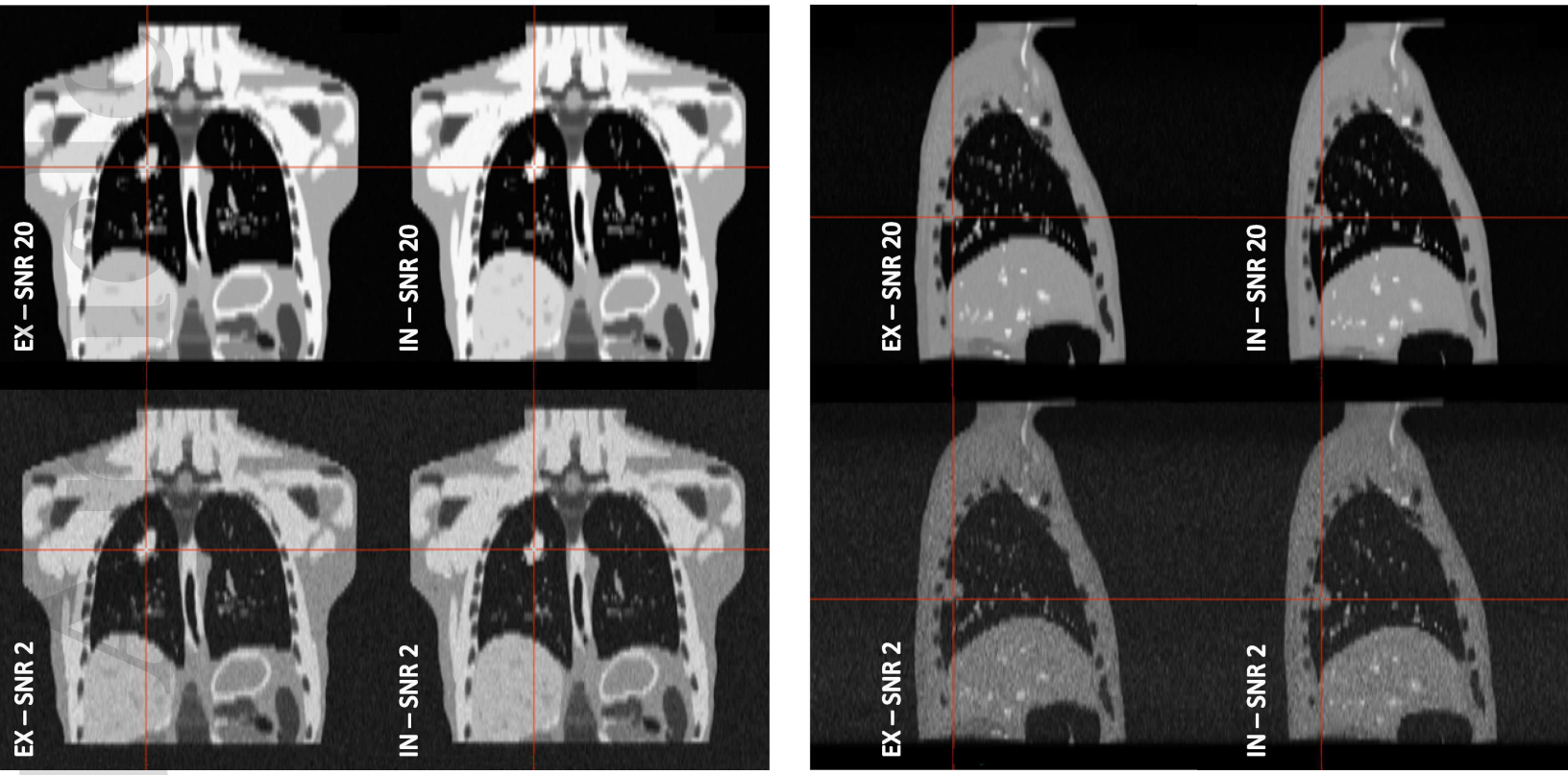

mp_14611_f7.eps